PRediction Of Geospace Radiation Environment and Solar wind parameterS

Work Package 4
Development of new statistical wave models and the re-estimation of the quasi-linear diffusion coefficients

Deliverable 4.3
Error reduction ratio analysis

Richard Boynton, Michael Balikhin, Simon Walker, Vladimir Krasnoselskikh, Yuri Shprits, Vitalii Shastun, Oleksiy Agapitov

November 3, 2015

This project has received funding from the *European Union's Horizon 2020 research and innovation programme* under grant agreement No 637302.

Document Change Record

Issue	Date	Author	Details
1.0	30/10/2015	R. J. Boynton	Initial draft

1 Introduction

Work Package 4 is devoted to the development of a new statistical wave model, which can be used to estimate the quasi-linear diffusion coefficients within numerical models that simulate the radiation belt environment. Currently, the statistical models of such waves are parameterised by the location and geomagnetic indices. This assumes that the preceding state of the magnetosphere plays no role in the current wave distribution in the magnetosphere. Also, it is known that electron fluxes at GEO are influenced more by solar wind velocity and density than that of the geomagnetic indices. Therefore, such parameters that are statistically related to the fluences of electrons should also be included in the development of statistical wave models. The initial problems to making such a model is to identify the solar wind parameters and geomagnetic indices that effect the wave distribution in a particular location and determine the time delay between cause and effect. The Error Reduction Ratio (ERR) analysis, which is key in the development of Nonlinear Auto-Regressive Moving Average eXogenous input (NARMAX) models, can solve both these problems and is employed in this study.

The main goal of this deliverable is to identify the geomagnetic and solar wind influence on different emissions within the inner magnetosphere. The ERR analysis is employed to identify these control parameters and determine the significant time lag. The emissions that we are concerned with for this study are lower band chorus, hiss and equatorial magnetosonic waves.

2 Conclusion

The results presented in this study show that while the AE and Dst index control the largest proportion of the emissions variance, the solar wind parameters also have a significant contribution to the emissions variance according to the ERR analysis.

The statistical wave models that have previously been employed within numerical codes also have no definitive answer for the lag of the geomagnetic indices that should be used to organise models. The results from the ERR analysis have identified the significant lags to use for both geomagnetic indices and solar wind parameters.

JOURNAL OF GEOPHYSICAL RESEARCH, VOL. ???, XXXX, DOI:10.1029/,

The influence of solar wind and geomagnetic indices on emissions in the magnetosphere: Lower Band Chorus, Hiss and Equatorial Magnetosonic waves

R. J. Boynton,[1] M. A. Balikhin,[1] S. N. Walker,[1] V. Krasnoselskikh,[2] Y. Shprits,[3] Vitalii Shastun,[2] O. Agapitov,[2]

R. J. Boynton, Department of Automatic Control and Systems Engineering, University of Sheffield, Mappin Street, Sheffield S1 3JD, UK. (r.boynton@sheffield.ac.uk)

[1]Department of Automatic Control and Systems Engineering, University of Sheffield, Sheffield S1 3JD, United Kingdom.

[2]LPCE/CNRS and Université d'Orléans, Orléans, France

[3]UCLA, LA, USA

Abstract. Statistical wave models, describing the distribution of wave amplitudes as parameters such as location and geomagnetic activity, are needed as the basis to describe the wave particle interactions within models of the radiation belts. In this study, we widen the scope of the statistical wave models by investigating which of the solar wind parameters or geomagnetic indices have the greatest influence on plasma waves in the radiation belts. The three emission types analysed in this study were Lower Band Chorus (LBC), Hiss and Equatorial MagnetoSonic (EMS) waves. The solar wind parameters or geomagnetic indices with the greatest control over the waves were found using the Error Reduction Ratio (ERR) analysis, which plays a key role in system identification modelling techniques. In this application, the wave magnitudes for the three emission types at different locations are considered as the output data, while the solar wind parameters and geomagnetic indices are the input data. The ERR analysis automatically determines a set of the most influential parameters that explain the variations in the emissions. The results show that the majority of the variation in emissions may be attributed to geomagnetic activity, such as the variation in the AE index. However, the results also show that the solar wind parameters also explain a significant proportion of the variance, such as solar wind velocity, which has a significant ERR in many of the locations that were analysed.

1. Introduction

Highly energetic electrons were observed by *Van Allen* [1959] during the first in situ space radiation measurements, leading to the discovery of the radiation belts. High fluences of these electrons have been known to cause serious problems to the satellites that transit this region. These problems can range from single event upsets, from which the spacecraft will recover, to the total failure of the satellite [*Blake et al.*, 1992]. With prior warning of when these high fluences are expected to occur it is possible for satellite operators to mitigate some of the damaging effects of these electrons.

To forecast these events a reliable model of the radiation belt system is required, which can accurately forecast the magnitude of the electron fluxes. Electron flux models based on first principles, such as Versatile Electron Radiation Belt (VERB) [*Subbotin et al.*, 2011], employ numerical codes that involve finding solutions of the diffusion equations. Within these codes, the tensors of the quasilinear diffusion coefficients need to be calculated to estimate the effects of the various wave modes on the energy and pitch angle scattering. To accurately evaluate these tensor diffusion coefficients for the VERB code, statistical wave models for Lower Band Chorus (LBC), Hiss and Equatorial MagnetoSonic (EMS) waves are used.

Chorus emissions are electromagnetic waves found outside the plasmapause near the geomagnetic equator [*Burtis and Helliwell*, 1969; *Santolík et al.*, 2005; *Li et al.*, 2011]. They are observed in two frequency bands, above and below half the electron gyrofrequency [*Helliwell*, 1967; *Tsurutani and Smith*, 1974; *Agapitov et al.*, 2013]. These waves have been shown to interact with the population of electrons within the radiation belts, resulting in electron acceleration and also the loss of electrons by pitch angle scattering into the loss cone [*Bortnik and Thorne*, 2007; *Shprits et al.*, 2008; *Mourenas et al.*, 2012; *Artemyev et al.*, 2013; *Mourenas et al.*, 2014]. The effect of upper band chorus waves on energetic electrons have been shown to be significantly lower than that of LBC [*Meredith et al.*, 2001; *Haque et al.*, 2010] and so is not included in this study.

Plasmaspheric hiss are electromagnetic waves that occur within high density regions of the plasmasphere and have a frequency range of 100 Hz to several kHz. Hiss waves are known to cause pitch angle scattering over a wide range of electron energies and L-shells and thus lead to the precipitation of the electron through the loss cone [*Meredith et al.*, 2006; *Summers et al.*, 2007; *Orlova et al.*, 2014].

The electromagnetic EMS waves are whistler mode emissions that propagate almost perpendicular with respect to the external magnetic field and are spatially confined to within a few degrees of the geomagnetic equator, both inside and outside the plasmasphere [*Russell et al.*, 1970; *Laakso et al.*, 1990; *Santolík et al.*, 2002]. They are observed between the proton gyrofrequency and the lower hybrid resonance frequency and generated as a result of proton ring distributions [*Perraut et al.*, 1982; *Boardsen et al.*, 1992; *Chen et al.*, 2011; *Ma et al.*, 2014; *Balikhin et al.*, 2015]. It has been shown that EMS waves are able to interact with electrons through Landau resonance and accelerate electrons to relativistic speeds *Horne et al.* [2007].

Currently, the statistical models of such waves are parameterised by the location of observations and current values for geomagnetic indices. This assumes that the preceding state of the magnetosphere plays no role in the current wave distribution in the magnetosphere. Also, it is known that electron fluxes at Geostationary Earth Orbit (GEO) are influenced more by changes in the solar wind velocity and density than that of the geomagnetic indices [*Paulikas and Blake*, 1979; *Blake et al.*, 1997; *Reeves et al.*, 2011; *Balikhin et al.*, 2011; *Boynton et al.*, 2013]. Therefore, such parameters that are statistically related to the fluences of electrons should also be included in the development of statistical wave models. The initial problems of developing such a model is to identify the solar wind parameters and geomagnetic indices that have the greatest influence on the wave distribution at a particular location and to determine the time delay between cause and effect.

The Error Reduction Ratio (ERR) analysis, which is key in the development of Nonlinear Auto-Regressive Moving Average eXogenous input (NARMAX) models, can solve both these problems. The ERR analysis is able to assess the influence of different inputs with different time lags on the measured output. It was first developed by *Billings et al.* [1988] in the field of system identification to determine the most influential inputs to a NARMAX model. It has since been employed in a wide range of fields, from modelling the tide in the Venice Lagoon [*Wei and Billings*, 2006] to analysing the adaptive changes in the photoreceptors of Drosophila flies [*Friederich et al.*, 2009]. In the field of space physics, the ERR analysis has been used to develop models for the Dst index [*Boaghe et al.*, 2001; *Balikhin et al.*, 2001; *Boynton et al.*, 2011a] and the electron fluxes at GEO [*Wei et al.*, 2011; *Boynton et al.*, 2015]. Due to the on going question of which solar wind-magnetosphere coupling function controls the Dst index, *Boynton et al.* [2011b] employed the ERR analysis to deduce a solar wind-magnetosphere coupling function. The advantage of the ERR analysis is that it can automatically combine inputs, cross-coupling them into a nonlinear function. The technique of employing the ERR to automatically determine the most influential inputs to a system was also applied to a wide range of electron flux energies at GEO [*Balikhin et al.*, 2011; *Boynton et al.*, 2013]. These studies found that the solar wind density plays a significant role in the dynamics of the high energy electrons (> 1 MeV). In addition, the ERR results showed the existence of a relationship between the time lags of the solar wind velocity and the energy of the electrons and thus allowed *Balikhin et al.* [2012] to compare this with the energy diffusion equation, leading to the conclusion that electron acceleration due to local diffusion does not dominate at GEO.

The aims of this study are to determine the influential parameters that control the wave amplitude distribution at particular locations. The ERR analysis is employed to identify these control parameters from a set that includes solar wind variables and geomagnetic indices, and also to determine any significant time lags. The wave distributions that we are concerned with for this study are the same ones that are required for the VERB code: LBC, hiss and EMS waves. The first step in this study was to determine which particular locations to use for each emission type. This is discussed in Section 2 along with a description of the instrumentation and data employed for this study. Section 3 gives more detail on the ERR analysis and how it is utilised. The results are presented in Section 4 and discussed in Section 5. Finally the study is concluded in Section 6

2. Data and instrumentation

The solar wind data used for this study was obtained from OMNI website (http://omniweb.gsfc.nasa.gov). The 1-minute solar wind velocity, density and IMF data were then averaged over 1 hour. The AE index and Dst index were obtained from the World Data Center for Geomagnetism, Kyoto (http://wdc.kugi.kyoto-u.ac.jp/index.html). Here, the hourly Dst index was employed as input to the algorithm without modification, while the 1-minute AE index data were averaged over 1 hour.

The wave data used in this study come from the search coil magnetometer instruments onboard the Cluster [*Escoubet et al.*, 1997] and THEMIS [*Angelopoulos*, 2008] spacecraft during the periods February 2001 to December 2010 and January 2008 to December 2014 respectively. The Cluster STAFF-SA (Spatio-Temporal Analysis of Field Fluctuations Spectrum Analyser) [*Cornilleau-Wehrlin et al.*, 1997] measured magnetic field oscillations in the frequency range 8 Hz to 4 kHz using 27 logarithmically spaced frequency channels and a sampling rate in the range of 1 to 8 Hz. THEMIS data come from the search coil magnetometer (SCM) [*Roux et al.*, 2008] on satellites A, D, and E. SCM was designed to investigate magnetic field oscillations in the frequency range 0.1 Hz to 4 kHz in 6 frequency bands (filter bank mode) and sampling rates between 1/16 to 8 Hz.

Each of the three emission types is observed in their own distinct frequency range. These frequency ranges were used to separate the different waves into three datasets, one for each emission. The three datasets contained the LBC, hiss and EMS wave magnitude in time, L-shell, Magnetic Local Time (MLT) and magnetic latitude.

The next step was to determine the spatial resolutions for each of the bins or sectors. This study only considered measurements in the vicinity of the equator for each of the emission types. Therefore the spatial dimensions in magnetic latitude was between -15° and 15°. The bin size for the other two spatial dimensions was determined by data availability. Initially, the number of satellite tracks in each spacial bin covering 1 hour MLT and 1 R_E radially (with a range of 3-7 R_E) was determined. These spatial bins were then combined first radially into 2 bins covering $4 \leq L \leq 5$ and $5 < L \leq 7$ and then secondly by MLT such that each of the spatial bins would contain over 1000 data points. This criteria arises due to the fact that the ERR analysis requires around 1000 data points, covering a wide range of conditions, for reliable results. The final set of data bins employed for this study are shown in Table 1 for LBC, Table 2 for Hiss and Table 3 for EMS. Note that in Tables 2 and 3 there are bins that overlap each other, for example the Hiss bins between 20-00 MLT and 22-04 MLT. The reason for this is that a single bin covering 00-04 MLT would not contain enough data for the ERR analysis to perform reliably.

Once all the spatial resolutions for the bins were determined, a 1-hour resolution time series dataset was constructed for each wave types at each selected location. With each of the spatial bins, the data point at time t was the maximum wave magnitude between the start of the hour and just before the start of the next hour. If no satellite measured the wave magnitude within the spatial bin for time t then the value was set to not a number and the ERR analysis would exclude this data point within the algorithm. Since the satellite coverage for the desired spatial bins was sparse, the majority of the datasets were data gaps.

3. Methodology

The methodology employed for this study is the ERR analysis, which plays a pivotal role in identifying a NARMAX model [*Leontaritis and Billings*, 1985a, b] and is based on the Forward Regression Orthogonal Least Squares (FROLS) algorithm [*Billings et al.*, 1988]. A single output multi input NARMAX model can be represented as Eq. (1)

$$
\begin{aligned}
y(t) \;=\; & F[y(t-1), ..., y(t-n_y), \\
& u_1(t-1), ..., u_1(t-n_{u_1}), ..., \\
& u_m(t-1), ..., u_m(t-n_{u_m}), ..., \\
& e(t-1), ..., e(t-n_e)] + e(t) \qquad (1)
\end{aligned}
$$

where y at time t is the output parameter that is to be modelled as some nonlinear function, F, of past outputs, past inputs u (where 1,...,m represent m different inputs), and past error terms e. Here, n_y, n_{u_1}, ..., n_{u_m} and n_e are the maximum lags for the output, m inputs and error terms.

If Equation (1) is set to be a polynomial with a cubic degree of nonlinearity and the maximum lags of the output, 6 inputs, and error terms is set to 10, then there will be 43680 monomials within the polynomial. The vast majority of these monomials will have a negligible influence on the output and thus the coefficient attached to these monomials will be zero. The majority of the variance of y can usually be explained by a few monomials and the FROLS algorithm is able to deduce and rank these significant monomials from the input and output data. This makes the FROLS algorithm highly useful for determining the parameters that influence the system, since with this study, we are not sure which solar wind and geomagnetic conditions lead to the waves within the inner magnetosphere.

The FROLS algorithm ranks each candidate monomial by its ERR. The ERR of a monomial represents the proportion (or percentage) of the output variance that is accounted for by that particular monomial. The process that is used to determine the ERR involves an iterative forward regression methodology and proceeds as follows. During the first iteration, the ERR is calculated for each of the candidate monomials with respect to the output data set. The monomial with the highest value of ERR is selected as the first model term and the remaining monomials are then orthogonalised with respect to the selected monomial using a Gram-Schmidt process. A second iteration is then performed on the remaining orthogonalised monomials, calculating a new set of ERR values, extracting the highest term. The third iteration orthogonalises the remaining terms with respect to both the first and second monomials identified. This processes of orthogonalisation with respect to the previously determined subspaces continues until the desired number of monomial terms has been selected. With each additional monomial selected, an increasing amount of the variance of the dependant variable is accounted for, i.e., the sum of the ERR, and thus the ratio of error to signal is reduced. The orthogonalisation allows for the individual contribution of each monomial to be determined. The full details of the FROLS algorithm is beyond the scope of this paper but detailed explanations of the algorithm can be found in *Billings et al.* [1989] or *Boynton et al.* [2011b].

For this study, wave emission data in a location described in MLT and L-shell are taken as the output data. The ERR analysis was then run for each location bin and for each wave type mentioned in Section 2. The same inputs were used for each of the 33 datasets, namely the solar wind velocity, density and dynamic pressure, the Dst index, the AE index and the IMF factor of the coupling function proposed by *Balikhin et al.* [2010] and *Boynton et al.* [2011b], $B_T \sin^6(\theta/2)$ (where $B_T = \sqrt{(B_y^2 + B_z^2)}$ is the tangential IMF and $\theta = \tan^{-1}(B_y/B_z)$ is the clock angle of the IMF).

For each of the output datasets (characterised by wave type, MLT and L-shell), there are many data gaps because it is impossible for the satellites to monitor each location all the time. As a result, there are very few cases for which there is sufficient data to assess the contribution of the previous output value to the system, i.e., if the system has a memory. Therefore, when the previous emission value is included in the search, there are very few data points to calculate the ERR and the results would not be reliable. As such, all auto-regressive terms in Equation (1) were removed from the search. The error terms were also excluded from the search for the same reason. This leaves only monomials consisting of the linear and nonlinear combinations of the exogenous inputs to be considered as candidates in the search. For each output dataset, the maximum number of lags was set to be 10 hours, while the degree of the polynomial was set to 1 to allow for a simpler analysis of the results. In a separate test the degree was set to 2 to identify any quadratic nonlinear combinations of the inputs.

4. ERR analysis results

The results of the ERR analysis for the three emission types at the different locations and for both a polynomial degree of 1 and 2 can be found in the appendix (Tables 4-36). Figures 1, 2, and 3 were constructed to compare the linear ERR results in a simpler manner for the three wave types. The Figures 1-3 show a polar representation of the inner magnetosphere with L-shell as radial distance and MLT as azimuth. Each spatial bin used in the analysis is delineated by a white boarder. For each individual sector, there are two colours that represent the top two control parameters of the emission type according to their ERR. The radial width of each coloured segment is proportional to the parameters relative contribution to the emission, i.e., if there ERR of the top parameter was 20% and the second parameter was 10% then the colour of the top parameter would be in outer two thirds of the radial distance for that sector while the colour for the second parameter would be in the remaining third.

Each of the 6 parameters is represented by a different colour. The solar wind velocity is indicated by red, the density by yellow and the pressure by green. Blue represents the Dst index and magenta the AE index. The IMF factor from the coupling function proposed by *Balikhin et al.* [2010] and *Boynton et al.* [2011b] is cyan. The effective lag of the control parameter is also depicted the Figures where darker colours signify a larger time lag.

4.1. LBC wave distribution

Figure 1 shows the top two linear control parameters for LBC waves in each of the 10 sectors analysed. The results show that either the AE index, Dst index or solar wind velocity have the largest ERR in all the sectors.

The AE index has the largest control over the LBC from just before midnight to midday in the inner sectors between L-shells 4 and 5 and also has an influence in the afternoon sector, with time delays of 1 hour pre-noon and a 2 hour lag for the afternoon sector. The AE index also plays a significant role in the outer L-shells analysed in this study (between L=5-7). It has the largest ERR from 04 MLT to midday in the outer sectors, with a lag of 1 hour at dawn and 2 hours pre-noon. A 1 hour delay of the AE index also has significant influence in the outer night sector.

The Dst index has the largest ERR in all the afternoon and dusk sectors, with a two hour lag in the afternoon that increases to 9 and 4 hours for the inner and outer dusk sectors respectively.

The solar wind velocity with a 9 hour lag has the most control in the outer night sector according to ERR. It is also the second parameter in the other sectors apart from at dusk and in the inner afternoon sector (where it is the third parameter). In the dusk sectors the solar wind density and IMF factor are the second parameters for the inner and outer bins respectively.

The ERR of a parameter explains the proportion of the dependant variable variance of the wave magnitude. Therefore, large differences in the sum of the ERR of the two parameters, $\sum \mathrm{ERR}_{1-2}$, between each sector should be noted. This can be found from Tables 4-36. For instance, $\sum \mathrm{ERR}_{1-2}$ in the dusk sectors is much less than that of the dawn sector where the highest $\sum \mathrm{ERR}_{1-2}$ is found. The inner sectors also have a higher $\sum \mathrm{ERR}_{1-2}$ than the outer sectors apart from in the pre-noon sector.

4.2. Hiss wave distribution

Figure 2 shows the top two linear control parameters for Hiss waves in each of the 12 sectors analysed. The grey line at 22 MLT indicates that sectors anticlockwise of the two sectors with the grey line striking through them, should extend from 22 MLT to 04 MLT due to the bins overlapping, as discussed in Section 2. For Hiss emissions, AE index, IMF Factor and Dst index have the largest ERR in different sectors.

From 08 MLT to 20 MLT, the AE index is the parameter with the highest ERR. The time lags of the AE index increase from the pre noon sectors going anticlockwise to the dusk sector. The lags increase from 1 hour to 3 hours to 6 hours in the inner sectors and from 1 hour to 2 hours to 8 hours in the outer sectors.

The IMF factor has the largest influence with respect to ERR from 22 MLT to 08 MLT, with no obvious patten in time lags, which are between 1 and 3 hours. The Dst index has the highest ERR in the two pre-midnight sectors, both with a lag of 1 hour.

The solar wind velocity has the second highest ERR from midnight to the afternoon sector, apart from in the inner dawn sector where it was the solar wind density. The solar wind density was also the second parameter in the dusk sectors, while it was the dynamic pressure in the pre midnight sector.

For Hiss waves, there is not as big a difference in $\sum \mathrm{ERR}_{1-2}$ between highest and lowest sectors. Again, the lowest $\sum \mathrm{ERR}_{1-2}$ is in the outer dusk sector, while the highest $\sum \mathrm{ERR}_{1-2}$ is in the outer dawn sector, however, the inner dawn sector has the second lowest $\sum \mathrm{ERR}_{1-2}$.

4.3. EMS wave distribution

Figure 3 shows the top two linear control parameters for EMS waves in each of the 11 sectors analysed. Again, the grey line in the sector at $L = 5 - 7$ and MLT=19-23, indicates that the adjacent sector anticlockwise should extend from 22 MLT to 05 MLT. As with Hiss waves, the top control parameters are AE index, Dst index and IMF factor according to the ERR. Due to maximising the amount of data in each sector to make the ERR analysis more reliable, the inner and outer sectors are not aligned.

The AE index controls the pre-noon and afternoon inside sectors and the noon and dusk outside sectors. The top two parameters for the pre-noon inside sector are both the AE index, the top parameter having a time lag of 6 hour and the second parameter having a 1 hour lag. Moving to the afternoon inside sector the AE index time lag becomes 3 hours.

The outside noon sector has a 1 hour lag, which increases to 2 hours for the dusk sector. The AE index also has the second highest ERR in the outside dawn sector.

The Dst index has the most control of EMS waves in the inside sectors from 16 MLT to 4 MLT, which have long time lags of 9-10 hours, apart from the dusk sector, which is 1 hour. It is also the second parameter for the inside dawn sector. The Dst index has the highest ERR for the two outer night time sectors between 19 MLT and 05 MLT. The sector on the morning side has a Dst time lag of 1 hour, while the evening sector has a 3 hour Dst index lag.

Both outer and inner sectors around dawn are controlled by the IMF factor with time lags of 6 and 7 hours. The IMF is also has the second highest ERR in the inside sectors from dusk to early morning and outside sector from late evening to early morning. The solar wind density is the second parameter in the sectors around noon and afternoon.

EMS waves have the smallest $\sum \mathrm{ERR}_{1-2}$ of the three emission types studied with the highest in the inner afternoon sector and lowest at the outer dawn sector.

5. Discussion

The aim of this study was to determine which the solar wind and geomagnetic parameters have the greatest influence on the LBC, Hiss and EMS emissions. This knowledge is needed to develop better statistical wave models, which may subsequently be used to evaluate the tensors of the quasilinear diffusion coefficients within electron flux models such as VERB [*Subbotin et al.*, 2011]. Current statistical wave models only use geomagnetic indices and do not take into account time delays. This study assesses both solar wind and geomagnetic parameters with up to 10 hours of lag, which should better account for the dynamical processes within the outer radiation belt. Therefore, the results of this study will potentially lead to more reliable wave models and in-turn better forecasts of electron fluxes in the radiation belts from first principles based tools such as VERB.

The results for LBC emissions are comparable with previous studies that compared wave distributions to geomagnetic indices [*Meredith et al.*, 2003; *Li et al.*, 2011; *Meredith et al.*, 2012; *Agapitov et al.*, 2013; *Aryan et al.*, 2014]. These results found a strong relationship with geomagnetic indices, while the results from *Aryan et al.* [2014] showed some dependency with solar wind parameters. *Aryan et al.* [2014] found that intense LBC occur at times when the AE index, solar wind velocity, and dynamic pressure are high, the solar wind density is low and the z-component of the IMF is southward. However, identifying the correct set of parameters that control the LBC wave magnitudes is more complex because it is well known that geomagnetic indices have a strong relationship with solar wind parameters. Therefore, high wave intensities during periods of high solar wind velocity may be due to the high solar wind velocity increasing the geomagnetic activity. The ERR is able to separate out the individual dependencies for each of the parameters and assess their contribution. For example, if the AE index is the actual cause of the emission variation and the solar wind velocity controls a large proportion of the AE index variation, then the velocity will only contribute to the wave intensities as part of the AE index contribution. The ERR analysis should identify the AE index as the parameter with the strongest relationship with the wave intensity. When searching for the second parameter, the methodology will remove the velocity contribution associated with the AE index through the orthogonalisation discussed in Section 3. In this example, the velocity would not be selected as a parameter even if it had the second highest correlation (after AE index) with the wave intensities.

The results of the ERR analysis show that the AE index has a strong relationship with LBC waves in the same locations as the high intensity LBC waves observed by *Meredith et al.* [2003]. This spatial location also corresponds to where the largest sum of the ERR is found, which is logical since if there are larger variations in the signal then the signal to noise ratio ($1 - \sum$ERR) will be larger. The time lags indicate that these high intensity LBC emissions are generated all across the dusk side of the inner magnetosphere 1-2 hours after substorm activity measured through the AE index. For the high intensity locations observed by *Meredith et al.* [2003], the solar wind velocity with a 6-10 hour time lag also has a significant dependance on LBC waves. Therefore, these results indicate that the velocity dependance showed by *Aryan et al.* [2014] is not simply acting through the AE index but should be included in statistical wave models.

The results for the hiss emissions show a dependance with AE index on the dayside, stretching from 08 MLT to 20 MLT. This corresponds to the locations of equatorial high intensity hiss observed by *Meredith et al.* [2004] during active geomagnetic conditions. There is an interesting pattern with the time lags of the AE index and the hiss wave intensity. In both of the pre-noon sectors between 08-12 MLT, the hiss activity has 1 hour time delay with AE index, then moving into the afternoon sector and then the dusk sector, the time lags of the AE index increase in steps. Again, as with LBC, the solar wind parameters have an independent role in influencing the hiss emissions according to the ERR, since they may be used to account for a significant proportion of the hiss variance. Therefore, such parameters should be included in statistical wave models and could potentially lead to better results for numerical diffusion code models.

The results from the EMS waves show a noon to dusk relationship with AE index, a nightside relationship with Dst index and a dawn relationship with IMF factor. Solar wind velocity, density and pressure also explain a significant proportion of the EMS waves according to the ERR analysis. As such these parameters should be included in statistical wave models.

The ERR was also set to search for any nonlinear influences on the emissions in a separate test, where the degree of the nonlinear exogenous inputs were set to be quadratic. These results are shown in Tables 4-36, where the identified linear parameters can be compared to the quadratic parameters selected by the ERR analysis. Each Table indicates an emission type for each sector, showing the ERR of the top five selected parameters for both the quadratic and linear search. In the majority of tables the parameter with the highest ERR in the linear test appears with the highest ERR in the quadratic test, however, often with another parameter coupled with it. The top parameter changes in only six sectors from all three wave types. Three of these change are from a linear Dst index to a combination of IMF factor and pressure, which is similar to the solar wind-Dst index coupling function proposed by *Boynton et al.* [2011b].

It should be noted that the spatial sizes of each of the sectors were compromised so that there was enough data to perform the ERR analysis. Sectors in hiss and EMS had to overlap so that there was adequate information. With more data availability of the wave magnitudes it would be possible to increase the spatial resolution of this type of analysis and perhaps improve the results.

6. Conclusions

This study has analysed the solar wind and geomagnetic influences for three emission types in the inner magnetosphere. Previously, statistical wave models used in numerical diffusion codes, have only considered geomagnetic influences, such as the AE index. The results presented in this study show that while the AE and Dst index control the largest proportion of the emissions variance, the solar wind parameters also have a significant contribution to the emissions variance according to the ERR analysis.

The statistical wave models that have previously been employed within numerical codes also have no definitive answer for the lag of the geomagnetic indices that should be used to organise models. The results from the ERR analysis have identified the significant lags to use for both geomagnetic indices and solar wind parameters for a wide range of locations in the inner magnetosphere.

This study had to compromise the size of the data bins or sectors to make sure that each sector had enough information to perform the ERR analysis. As such, with more data coverage from future missions that explore these emissions in the inner magnetosphere, we will be able to increase the spatial resolution of this type of analysis to yield more detailed results.

Acknowledgments. Solar wind data was obtained from OMNIweb (http://omniweb.gsfc.nasa.gov/ow_ Dst index and AE index data were from the World Data Center for Geomagnetism, Kyoto (http://wdc.kugi.kyoto-u.ac.jp/index.html). The Cluster STAFF data and the THEMIS SCM was provided by LPC2E. This project has received funding from the European Union's Horizon 2020 research and innovation programme under grant agreement No 637302.

References

Agapitov, O., A. Artemyev, V. Krasnoselskikh, Y. V. Khotyaintsev, D. Mourenas, H. Breuillard, M. Balikhin, and G. Rolland, Statistics of whistler mode waves in the outer radiation belt: Cluster staff-sa measurements, *J. Geophys. Res. Space Physics*, *118*(6), 3407–3420, 2013.

Angelopoulos, V., The THEMIS mission, *Sp. Sci. Rev.*, *141*, 5–34, doi:10.1007/s11214-008-9336-1, 2008.

Artemyev, A. V., O. V. Agapitov, D. Mourenas, V. Krasnoselskikh, and L. M. Zelenyi, Storm-induced energization of radiation belt electrons: Effect of wave obliquity, *Geophys. Res. Lett.*, *40*(16), 4138–4143, 2013.

Aryan, H., K. Yearby, M. Balikhin, O. Agapitov, V. Krasnoselskikh, and R. Boynton, Statistical study of chorus wave distributions in the inner magnetosphere using ae and solar wind parameters, *J. Geophys. Res. Space Physics*, *119*(8), 6131–6144, 2014.

Balikhin, M. A., O. M. Boaghe, S. A. Billings, and H. S. C. K. Alleyne, Terrestrial magnetosphere as a nonlinear resonator, *Geophys. Res. Lett.*, *28(6)*, 11231126, 2001.

Balikhin, M. A., R. J. Boynton, S. A. Billings, M. Gedalin, N. Ganushkina, D. Coca, and H. Wei, Data based quest for solar wind-magnetosphere coupling function, *Geophys. Res. Lett.*, *37*(24), L24,107, 2010.

Balikhin, M. A., R. J. Boynton, S. N. Walker, J. E. Borovsky, S. A. Billings, and H. L. Wei, Using the narmax approach to model the evolution of energetic electrons fluxes at geostationary orbit, *Geophys. Res. Lett.*, *38*(18), L18,105, 2011.

Balikhin, M. A., M. Gedalin, G. D. Reeves, R. J. Boynton, and S. A. Billings, Time scaling of the electron flux increase at geo: The local energy diffusion model vs observations, *J. Geophys. Res.*, *117*(A10), A10,208–, 2012.

Balikhin, M. A., Y. Y. Shprits, S. N. Walker, L. Chen, N. Cornilleau-Wehrlin, I. Dandouras, O. Santolik, C. Carr, K. H. Yearby, and B. Weiss, Observations of discrete harmonics emerging from equatorial noise, *Nat Commun*, *6*, 1, doi:10.1038/ncomms8703, 2015.

Billings, S., M. Korenberg, and S. Chen, Identification of non-linear output affine systems using an orthogonal least-squares algorithm., *Int. J. of Systems Sci.*, *19*, 1559–1568, 1988.

Billings, S., S. Chen, and M. Korenberg, Identification of mimo non-linear systems using a forward-regression orthogonal estimator, *Int. J. Control*, *49(6)*, 2157–2189, 1989.

Blake, J. B., W. A. Kolasinski, R. W. Fillius, and E. G. Mullen, Injection of electrons and protons with energies of tens of mev into l¡3 on 24 march 1991, *Geophys. Res. Lett.*, *19*(8), 821–824, 1992.

Blake, J. B., D. N. Baker, N. Turner, K. W. Ogilvie, and R. P. Lepping, Correlation of changes in the outer-zone relativistic-electron population with upstream solar wind and magnetic field measurements, *Geophys. Res. Lett.*, *24*(8), 927–929, 1997.

Boaghe, O. M., M. A. Balikhin, S. A. Billings, and H. Alleyne, Identification of nonlinear processes in the magnetospheric dynamics and forecasting of dst index, *J. Geophys. Res.*, *106(A12)*, 30,04730,066, 2001.

Boardsen, S. A., D. L. Gallagher, D. A. Gurnett, W. K. Peterson, and J. L. Green, Funnel-shaped, low-frequency equatorial waves, *J. Geophys. Res.*, *97*(A10), 14,967–14,976, 1992.

Bortnik, J., and R. Thorne, The dual role of elf/vlf chorus waves in the acceleration and precipitation of radiation belt electrons, *Journal of Atmospheric and Solar-Terrestrial Physics*, *69*(3), 378–386, 2007.

Boynton, R. J., M. A. Balikhin, S. A. Billings, A. S. Sharma, and O. A. Amariutei, Data derived narmax dst model, *Annales Geophysicae*, *29*(6), 965–971, doi:10.5194/angeo-29-965-2011, 2011a.

Boynton, R. J., M. A. Balikhin, S. A. Billings, H. L. Wei, and N. Ganushkina, Using the narmax ols-err algorithm to obtain the most influential coupling functions that affect the evolution of the magnetosphere, *J. Geophys. Res.*, *116*(A5), A05,218, 2011b.

Boynton, R. J., M. A. Balikhin, S. A. Billings, G. D. Reeves, N. Ganushkina, M. Gedalin, O. A. Amariutei, J. E. Borovsky, and S. N. Walker, The analysis of electron fluxes at geosynchronous orbit employing a narmax approach, *J. Geophys. Res. Space Physics*, *118*(4), 1500–1513, 2013.

Boynton, R. J., M. A. Balikhin, and S. A. Billings, Online narmax model for electron fluxes at geo, *Ann. Geophys.*, *33*(3), 405–411, 2015.

Burtis, W. J., and R. A. Helliwell, Banded chorus - new type of vlf radiation observed in the magnetosphere by ogo 1 and ogo 3, *J. Geophys. Res.*, *74*(11), 3002–3010, 1969.

Chen, L., R. M. Thorne, V. K. Jordanova, M. F. Thomsen, and R. B. Horne, Magnetosonic wave instability analysis for proton ring distributions observed by the lanl magnetospheric plasma analyzer, *J. Geophys. Res.*, *116*, A03223, doi:10.1029/2010JA016068, 2011.

Cornilleau-Wehrlin, N., P. Chauveau, S. Louis, A. Meyer, J. Nappa, S. Perraut, L. Rezeau, P. Robert, A. Roux, C. De Villedary, Y. De Conchy, L. Friel, C. Harvey, D. Hubert,

C. Lacombe, R. Manning, F. Wouters, F. Lefeuvre, M. Parrot, J. Pinon, B. Poirier, W. Kofman, and P. Louarn, The cluster spatio-temporal analysis of field fluctuations (STAFF) experiment, *Space Sci. Rev.*, *79*(1-2), 107–136–, 1997.

Escoubet, C. P., R. Schmidt, and M. L. Goldstein, Cluster - Science and mission overview, *Sp. Sci. Rev.*, *79*, 11–32, 1997.

Friederich, U., D. Coca, S. A. Billings, and M. Juusola, Data modelling for analysis of adaptive changes in fly photoreceptors, *NEURAL INFORMATION PROCESSING, PT 1, PROCEEDINGS*, *5863*, 34–38, 2009.

Haque, N., M. Spasojevic, O. Santolk, and U. S. Inan, Wave normal angles of magnetospheric chorus emissions observed on the polar spacecraft, *J. Geophys. Res.*, *115*(A4), A00F07–, 2010.

Helliwell, R. A., A theory of discrete vlf emissions from the magnetosphere, *J. Geophys. Res.*, *72*(19), 4773–4790, 1967.

Horne, R. B., R. M. Thorne, S. A. Glauert, N. P. Meredith, D. Pokhotelov, and O. Santolk, Electron acceleration in the van allen radiation belts by fast magnetosonic waves, *Geophys. Res. Lett.*, *34*(17), L17,107, 2007.

Laakso, H., H. Junginger, A. Roux, R. Schmidt, and C. de Villedary, Magnetosonic waves above fc (h+) at geostationary orbit: Geos 2 results, *J. Geophys. Res.*, *95*(A7), 10,609–10,621, 1990.

Leontaritis, I. J., and S. A. Billings, Input-output parametric models for non-linear systems part i: Deterministic non-linear systems., *Int. J. Control*, *41 (2)*, 303–328, 1985a.

Leontaritis, I. J., and S. A. Billings, Input-output parametric models for non-linear systems part ii: Stochastic nonlinear systems, *Int. J. Control*, *41 (2)*, 329–344, 1985b.

Li, W., J. Bortnik, R. M. Thorne, and V. Angelopoulos, Global distribution of wave amplitudes and wave normal angles of chorus waves using themis wave observations, *J. Geophys. Res.*, *116*(A12), A12,205–, 2011.

Ma, Q., W. Li, L. Chen, R. M. Thorne, and V. Angelopoulos, Magnetosonic wave excitation by ion ring distributions in the earth's inner magnetosphere, *J. Geophys. Res.*, *119*, 844–852, doi:10.1002/2013JA019591, 2014.

Meredith, N. P., R. B. Horne, and R. R. Anderson, Substorm dependence of chorus amplitudes: Implications for the acceleration of electrons to relativistic energies, *J. Geophys. Res.*, *106*(A7), 13,165–13,178, 2001.

Meredith, N. P., M. Cain, R. B. Horne, R. M. Thorne, D. Summers, and R. R. Anderson, Evidence for chorus-driven electron acceleration to relativistic energies from a survey of geomagnetically disturbed periods, *J. Geophys. Res.*, *108*(A6), 1248–, 2003.

Meredith, N. P., R. B. Horne, R. M. Thorne, D. Summers, and R. R. Anderson, Substorm dependence of plasmaspheric hiss, *J. Geophys. Res.*, *109*(A6), A06,209–, 2004.

Meredith, N. P., R. B. Horne, S. A. Glauert, R. M. Thorne, D. Summers, J. M. Albert, and R. R. Anderson, Energetic outer zone electron loss timescales during low geomagnetic activity, *J. Geophys. Res.*, *111*(A5), A05,212–, 2006.

Meredith, N. P., R. B. Horne, A. Sicard-Piet, D. Boscher, K. H. Yearby, W. Li, and R. M. Thorne, Global model of lower band and upper band chorus from multiple satellite observations, *J. Geophys. Res.*, *117*(A10), A10,225–, 2012.

Mourenas, D., A. V. Artemyev, J.-F. Ripoll, O. V. Agapitov, and V. V. Krasnoselskikh, Timescales for electron quasi-linear diffusion by parallel and oblique lower-band chorus waves, *J. Geophys. Res.*, *117*(A6), A06,234–, 2012.

Mourenas, D., A. V. Artemyev, O. V. Agapitov, and V. Krasnoselskikh, Consequences of geomagnetic activity on energization and loss of radiation belt electrons by oblique chorus waves, *J. Geophys. Res. Space Physics*, *119*(4), 2775–2796, 2014.

Orlova, K., M. Spasojevic, and Y. Shprits, Activity-dependent global model of electron loss inside the plasmasphere, *Geophys. Res. Lett.*, *41*(11), 2014GL060,100–, 2014.

Paulikas, G. A., and J. B. Blake, Effects of the solar wind on magnetospheric dynamics: Energetic electrons at the synchronous orbit, *Quantitative Modeling of Magnetospheric Processes, Geophys. Monogr. Ser.*, *21*, 180–202, aGU, Washington, D. C., 1979.

Perraut, S., A. Roux, P. Robert, R. Gendrin, J. A. Sauvaud, J. M. Bosqued, G. Kremser, and A. Korth, A systematic study of ulf waves above f_{H^+} from geos 1 and 2 measurements and their relationship with proton ring distributions, *J. Geophys. Res.*, *87*, 6219, 1982.

Reeves, G. D., S. K. Morley, R. H. W. Friedel, M. G. Henderson, T. E. Cayton, G. Cunningham, J. B. Blake, R. A. Christensen, and D. Thomsen, On the relationship between relativistic electron flux and solar wind velocity: Paulikas and blake revisited, *J. Geophys. Res.*, *116*(A2), A02,213, 2011.

Roux, A., O. Le Contel, C. Coillot, A. Bouabdellah, B. de la Porte, D. Alison, S. Ruocco, and M. Vassal, The search coil magnetometer for themis, *Space Sci. Rev.*, *141*(1-4), 265–275–, 2008.

Russell, C. T., R. E. Holzer, and E. J. Smith, Ogo 3 observations of elf noise in the magnetosphere: 2. the nature of the equatorial noise, *J. Geophys. Res.*, *75*(4), 755–768, 1970.

Santolík, O., E. Macúšová, K. H. Yearby, N. Cornilleau-Wehrlin, and H. S. K. Alleyne, Radial variation of whistler-mode chorus: first results from the staff/dwp instrument on board the double star tc-1 spacecraft, *Ann. Geophys.*, *23*(8), 2937–2942, 2005.

Santolík, O., O., J. S. Pickett, D. A. Gurnett, M. Maksimovic, and N. Cornilleau-Wehrlin, Spatiotemporal variability and propagation of equatorial noise observed by cluster, *J. Geophys. Res.*, *107*(A12), 1495–, 2002.

Shprits, Y. Y., D. A. Subbotin, N. P. Meredith, and S. R. Elkington, Review of modeling of losses and sources of relativistic electrons in the outer radiation belt ii: Local acceleration and loss, *Journal of Atmospheric and Solar-Terrestrial Physics*, *70*(14), 1694–1713, 2008.

Subbotin, D. A., Y. Y. Shprits, and B. Ni, Long-term radiation belt simulation with the verb 3-d code: Comparison with crres observations, *J. Geophys. Res.*, *116*(A12), A12,210–, 2011.

Summers, D., B. Ni, and N. P. Meredith, Timescales for radiation belt electron acceleration and loss due to resonant wave-particle interactions: 1. theory, *J. Geophys. Res.*, *112*(A4), A04,206–, 2007.

Tsurutani, B. T., and E. J. Smith, Postmidnight chorus: A substorm phenomenon, *J. Geophys. Res.*, *79*(1), 118–127, 1974.

Van Allen, J. A., The geomagnetically trapped corpuscular radiation, *J. Geophys. Res.*, *64*(11), 1683–1689, 1959.

Wei, H. L., and S. A. Billings, An efficient nonlinear cardinal b-spline model for high tide forecasts at the venice lagoon, *Nonlinear Processes In Geophysics*, *13*(5), 577–584, 2006.

Table 1. Table showing the spatial dimensions of each bin for LBC

L-Shell (R_E)	MLT				
4-5	04-08	08-12	12-16	16-22	22-04
5-7	04-08	08-12	12-16	16-22	22-04

Table 2. Table showing the spatial dimensions of each bin for hiss

L-Shell (R_E)	MLT					
4-5	04-08	08-12	12-16	16-20	20-00	22-04
5-7	04-08	08-12	12-16	16-20	20-00	22-04

Table 3. Table showing the spatial dimensions of each bin for EMS

L-Shell (R_E)	MLT					
4-5	00-04	04-08	08-12	12-16	16-20	20-00
5-7	05-11	11-15	15-19	19-23	22-05	

Wei, H.-L., S. A. Billings, A. Surjalal Sharma, S. Wing, R. J. Boynton, and S. N. Walker, Forecasting relativistic electron flux using dynamic multiple regression models, *Annales Geophysicae*, *29*(2), 415–420, doi:10.5194/angeo-29-415-2011, 2011.

Appendix A: ERR Tables

A1. LBC emissions

Tables 4-13 show the ERR analysis results for the top five linear and quadratic nonlinear control parameters for LBC emissions.

A2. Hiss emissions

Tables 14-25 show the ERR analysis results for the top five linear and quadratic nonlinear control parameters for Hiss emissions.

A3. EMS emissions

Tables 26-36 show the ERR analysis results for the top five linear and quadratic nonlinear control parameters for EMS emissions.

Table 4. Table showing the control parameters according to their ERR for LBC emissions at L-shell 4-5 and MLT 22-04

LBC wave at L = 4-5 and MLT = 22-04			
Linear		Quadratic Nonlinear	
Control Parameter	ERR(%)	Control Parameter	ERR(%)
AE(t-1)	11.52	AE(t-1)p(t-2)	13.70
V(t-10)	8.45	n(t-2)V(t-6)	4.52
Dst(t-4)	1.54	AE(t-1)V(t-10)	2.50
n(t-2)	1.16	Dst(t-1)AE(t-3)	1.71
p(t-2)	0.92	AE(t-1)AE(t-1)	1.51
$\sum$ERR	23.58	$\sum$ERR	23.93

Table 5. Table showing the control parameters according to their ERR for LBC emissions at L-shell 4-5 and MLT 04-08

LBC wave at L = 4-5 and MLT = 04-08			
Linear		Quadratic Nonlinear	
Control Parameter	ERR(%)	Control Parameter	ERR(%)
AE(t-1)	21.75	AE(t-1)AE(t-1)	23.46
V(t-7)	11.38	AE(t-1)p(t-1)	4.62
Dst(t-7)	2.08	V(t-7)	3.09
$B_T \sin^6(\theta/2)$(t-10)	0.91	n(t-1)	2.60
V(t-5)	0.41	AE(t-1)	1.95
$\sum$ERR	36.53	$\sum$ERR	35.72

Table 6. Table showing the control parameters according to their ERR for LBC emissions at L-shell 4-5 and MLT 08-12

LBC wave at L = 4-5 and MLT = 08-12			
Linear		Quadratic Nonlinear	
Control Parameter	ERR(%)	Control Parameter	ERR(%)
AE(t-1)	15.36	AE(t-1)V(t-2)	16.94
V(t-6)	7.86	V(t-2)	7.86
AE(t-2)	1.74	AE(t-4)p(t-10)	1.83
n(t-2)	1.01	AE(t-2)	0.95
$B_T \sin^6(\theta/2)$(t-10)	0.61	AE(t-1)AE(t-1)	0.68
$\sum$ERR	26.57	$\sum$ERR	28.26

Table 7. Table showing the control parameters according to their ERR for LBC emissions at L-shell 4-5 and MLT 12-16

LBC wave at L = 4-5 and MLT = 12-16			
Linear		Quadratic Nonlinear	
Control Parameter	ERR(%)	Control Parameter	ERR(%)
Dst(t-2)	11.01	Dst(t-3)AE(t-2)	13.84
AE(t-2)	3.69	AE(t-2)p(t-9)	2.08
V(t-10)	2.91	Dst(t-1)p(t-2)	1.93
n(t-9)	1.11	Dst(t-7)V(t-7)	1.80
p(t-9)	0.99	V(t-10)	1.51
$\sum$ERR	19.72	$\sum$ERR	21.16

Table 8. Table showing the control parameters according to their ERR for LBC emissions at L-shell 4-5 and MLT 16-22

LBC wave at L = 4-5 and MLT = 16-22			
Linear		Quadratic Nonlinear	
Control Parameter	ERR(%)	Control Parameter	ERR(%)
Dst(t-9)	3.77	Dst(t-9)V(t-3)	4.10
n(t-3)	1.53	n(t-3)	1.54
AE(t-7)	0.77	$B_T \sin^6(\theta/2)$(t-5)n(t-10)	1.09
$B_T \sin^6(\theta/2)$(t-5)	0.62	AE(t-7)V(t-3)	0.78
p(t-1)	0.39	Dst(t-1)$B_T \sin^6(\theta/2)$(t-9)	0.75
$\sum$ERR	7.07	$\sum$ERR	8.26

Table 9. Table showing the control parameters according to their ERR for LBC emissions at L-shell 5-7 and MLT 22-04

LBC wave at L = 5-7 and MLT = 22-04			
Linear		Quadratic Nonlinear	
Control Parameter	ERR(%)	Control Parameter	ERR(%)
V(t-9)	5.67	V(t-9)	5.94
AE(t-1)	5.21	AE(t-1)V(t-3)	5.66
Dst(t-10)	0.89	AE(t-1)AE(t-1)	2.21
$B_T \sin^6(\theta/2)$(t-1)	0.73	$B_T \sin^6(\theta/2)$(t-1)	2.19
p(t-7)	0.72	Dst(t-10)	0.82
$\sum$ERR	13.22	$\sum$ERR	16.81

Table 10. Table showing the control parameters according to their ERR for LBC emissions at L-shell 5-7 and MLT 04-08

LBC wave at L = 5-7 and MLT = 04-08			
Linear		Quadratic Nonlinear	
Control Parameter	ERR(%)	Control Parameter	ERR(%)
AE(t-1)	15.21	AE(t-1)V(t-1)	15.85
V(t-10)	10.16	V(t-10)	10.50
p(t-1)	1.68	$B_T \sin^6(\theta/2)$(t-1)	2.40
n(t-1)	0.90	AE(t-1)AE(t-1)	1.83
$B_T \sin^6(\theta/2)$(t-10)	0.57	V(t-10)V(t-10)	1.04
$\sum$ERR	28.52	$\sum$ERR	31.61

Table 11. Table showing the control parameters according to their ERR for LBC emissions at L-shell 5-7 and MLT 08-12

LBC wave at L = 5-7 and MLT = 08-12			
Linear		Quadratic Nonlinear	
Control Parameter	ERR(%)	Control Parameter	ERR(%)
AE(t-2)	16.33	AE(t-1)V(t-1)	17.15
V(t-10)	8.60	V(t-2)	8.61
AE(t-1)	2.20	AE(t-2)AE(t-2)	3.29
p(t-1)	1.10	AE(t-2)	2.39
n(t-1)	1.08	$B_T \sin^6(\theta/2)$(t-2)V(t-7)	1.14
$\sum$ERR	29.31	$\sum$ERR	32.58

Table 12. Table showing the control parameters according to their ERR for LBC emissions at L-shell 5-7 and MLT 12-16

LBC wave at L = 5-7 and MLT = 12-16			
Linear		Quadratic Nonlinear	
Control Parameter	ERR(%)	Control Parameter	ERR(%)
Dst(t-2)	6.20	AE(t-3)V(t-3)	6.91
V(t-10)	3.45	V(t-9)	2.90
AE(t-7)	1.39	AE(t-7)	2.56
$B_T \sin^6(\theta/2)$(t-1)	1.33	AE(t-3)AE(t-3)	2.23
AE(t-3)	1.16	AE(t-7)AE(t-7)	1.04
$\sum$ERR	13.52	$\sum$ERR	15.64

Table 13. Table showing the control parameters according to their ERR for LBC emissions at L-shell 5-7 and MLT 16-22

LBC wave at L = 5-7 and MLT = 16-22			
Linear		Quadratic Nonlinear	
Control Parameter	ERR(%)	Control Parameter	ERR(%)
Dst(t-4)	1.59	Dst(t-4)	1.59
$B_T \sin^6(\theta/2)$(t-1)	0.96	$B_T \sin^6(\theta/2)$(t-1)	0.96
p(t-1)	0.47	Dst(t-6)$B_T \sin^6(\theta/2)$(t-10)	0.62
n(t-2)	0.29	AE(t-1)$B_T \sin^6(\theta/2)$(t-1)	0.61
$B_T \sin^6(\theta/2)$(t-5)	0.21	AE(t-1)	0.46
$\sum$ERR	3.52	$\sum$ERR	4.25

Table 14. Table showing the control parameters according to their ERR for Hiss emissions at L-shell 4-5 and MLT 22-04

Hiss wave at L = 4-5 and MLT = 22-04			
Linear		Quadratic Nonlinear	
Control Parameter	ERR(%)	Control Parameter	ERR(%)
$B_T \sin^6(\theta/2)$(t-3)	6.36	$B_T \sin^6(\theta/2)$(t-3)p(t-1)	8.51
V(t-7)	2.39	n(t-7)V(t-2)	1.51
Dst(t-6)	1.52	Dst(t-8)p(t-4)	1.32
p(t-2)	1.17	V(t-4)	0.98
$B_T \sin^6(\theta/2)$(t-8)	0.90	p(t-2)p(t-2)	0.64
$\sum$ERR	12.35	$\sum$ERR	12.95

Table 15. Table showing the control parameters according to their ERR for Hiss emissions at L-shell 4-5 and MLT 04-08

Hiss wave at L = 4-5 and MLT = 04-08			
Linear		Quadratic Nonlinear	
Control Parameter	ERR(%)	Control Parameter	ERR(%)
$B_T \sin^6(\theta/2)$(t-1)	4.06	$B_T \sin^6(\theta/2)$(t-1)p(t-3)	4.86
n(t-8)	1.90	$B_T \sin^6(\theta/2)$(t-3)p(t-8)	1.70
AE(t-1)	1.26	$B_T \sin^6(\theta/2)$(t-8)n(t-1)	1.46
V(t-2)	0.76	n(t-5)	1.24
$B_T \sin^6(\theta/2)$(t-4)	0.75	Dst(t-9)AE(t-4)	1.17
$\sum$ERR	8.73	$\sum$ERR	10.43

Table 16. Table showing the control parameters according to their ERR for Hiss emissions at L-shell 4-5 and MLT 08-12

Hiss wave at L = 4-5 and MLT = 08-12			
Linear		Quadratic Nonlinear	
Control Parameter	ERR(%)	Control Parameter	ERR(%)
AE(t-1)	7.36	AE(t-1)AE(t-1)	7.81
V(t-2)	4.41	V(t-9)	4.21
AE(t-8)	0.53	AE(t-1)V(t-10)	0.79
$B_T \sin^6(\theta/2)$(t-9)	0.29	Dst(t-5)$B_T \sin^6(\theta/2)$(t-1)	0.64
AE(t-5)	0.28	AE(t-4)n(t-10)	0.62
$\sum$ERR	12.87	$\sum$ERR	14.07

Table 17. Table showing the control parameters according to their ERR for Hiss emissions at L-shell 4-5 and MLT 12-16

Hiss wave at L = 4-5 and MLT = 12-16			
Linear		Quadratic Nonlinear	
Control Parameter	ERR(%)	Control Parameter	ERR(%)
AE(t-3)	5.76	AE(t-3)$B_T \sin^6(\theta/2)$(t-5)	6.66
V(t-10)	3.59	AE(t-1)p(t-9)	1.53
AE(t-1)	1.33	Dst(t-10)Dst(t-10)	1.42
AE(t-5)	0.70	n(t-7)	1.13
n(t-2)	0.39	AE(t-3)	0.97
$\sum$ERR	11.77	$\sum$ERR	11.72

Table 18. Table showing the control parameters according to their ERR for Hiss emissions at L-shell 4-5 and MLT 16-20

Hiss wave at L = 4-5 and MLT = 16-20			
Linear		Quadratic Nonlinear	
Control Parameter	ERR(%)	Control Parameter	ERR(%)
AE(t-6)	4.73	AE(t-7)V(t-3)	5.72
n(t-2)	4.21	n(t-2)	3.62
Dst(t-10)	1.51	AE(t-5)n(t-3)	1.94
$B_T \sin^6(\theta/2)$(t-1)	1.46	Dst(t-10)p(t-7)	1.41
AE(t-4)	1.09	AE(t-7)$B_T \sin^6(\theta/2)$(t-1)	1.22
$\sum$ERR	13.01	$\sum$ERR	13.90

Table 19. Table showing the control parameters according to their ERR for Hiss emissions at L-shell 4-5 and MLT 20-00

Hiss wave at L = 4-5 and MLT = 20-00			
Linear		Quadratic Nonlinear	
Control Parameter	ERR(%)	Control Parameter	ERR(%)
Dst(t-1)	5.73	$B_T \sin^6(\theta/2)$(t-3)p(t-1)	8.36
p(t-1)	3.04	n(t-2)	2.43
V(t-10)	2.54	AE(t-9)n(t-4)	1.76
AE(t-9)	1.25	$B_T \sin^6(\theta/2)$(t-2)p(t-1)	1.29
V(t-4)	0.69	$B_T \sin^6(\theta/2)$(t-9)p(t-7)	0.93
$\sum$ERR	13.25	$\sum$ERR	14.77

Table 20. Table showing the control parameters according to their ERR for Hiss emissions at L-shell 5-7 and MLT 22-04

Hiss wave at L = 5-7 and MLT = 22-04			
Linear		Quadratic Nonlinear	
Control Parameter	ERR(%)	Control Parameter	ERR(%)
$B_T \sin^6(\theta/2)$(t-1)	5.20	AE(t-1)n(t-4)	7.53
V(t-10)	4.27	V(t-10)	3.84
p(t-3)	2.85	$B_T \sin^6(\theta/2)$(t-1)	1.45
Dst(t-1)	1.15	p(t-1)V(t-8)	1.13
AE(t-1)	0.34	$B_T \sin^6(\theta/2)$(t-1)n(t-2)	0.92
$\sum$ERR	13.80	$\sum$ERR	14.87

Table 21. Table showing the control parameters according to their ERR for Hiss emissions at L-shell 5-7 and MLT 04-08

Hiss wave at L = 5-7 and MLT = 04-08			
Linear		Quadratic Nonlinear	
Control Parameter	ERR(%)	Control Parameter	ERR(%)
$B_T \sin^6(\theta/2)$(t-2)	12.15	$B_T \sin^6(\theta/2)$(t-2)V(t-1)	12.93
V(t-10)	4.65	V(t-10)	5.17
AE(t-1)	2.27	AE(t-4)p(t-2)	1.40
V(t-1)	1.02	$B_T \sin^6(\theta/2)$(t-1)V(t-1)	1.00
n(t-3)	0.88	AE(t-7)$B_T \sin^6(\theta/2)$(t-4)	0.97
$\sum$ERR	20.96	$\sum$ERR	21.47

Table 22. Table showing the control parameters according to their ERR for Hiss emissions at L-shell 5-7 and MLT 08-12

Hiss wave at L = 5-7 and MLT = 08-12			
Linear		Quadratic Nonlinear	
Control Parameter	ERR(%)	Control Parameter	ERR(%)
AE(t-1)	9.45	AE(t-1)	9.45
V(t-10)	4.96	V(t-10)	4.96
p(t-2)	0.68	AE(t-1)AE(t-1)	1.92
AE(t-10)	0.55	AE(t-10)	1.23
AE(t-2)	0.51	V(t-8)V(t-8)	0.99
$\sum$ERR	16.15	$\sum$ERR	18.55

Table 23. Table showing the control parameters according to their ERR for Hiss emissions at L-shell 5-7 and MLT 12-16

Hiss wave at L = 5-7 and MLT = 12-16			
Linear		Quadratic Nonlinear	
Control Parameter	ERR(%)	Control Parameter	ERR(%)
AE(t-2)	5.61	AE(t-2)V(t-4)	5.74
V(t-7)	3.31	V(t-7)	3.05
n(t-4)	0.64	Dst(t-3)AE(t-2)	0.76
Dst(t-10)	0.50	$B_T \sin^6(\theta/2)$(t-6)V(t-10)	0.72
AE(t-6)	0.49	$B_T \sin^6(\theta/2)$(t-8)n(t-9)	0.58
$\sum$ERR	10.55	$\sum$ERR	10.85

Table 24. Table showing the control parameters according to their ERR for Hiss emissions at L-shell 5-7 and MLT 16-20

Hiss wave at L = 5-7 and MLT = 16-20			
Linear		Quadratic Nonlinear	
Control Parameter	ERR(%)	Control Parameter	ERR(%)
AE(t-8)	2.76	AE(t-8)V(t-4)	3.18
n(t-2)	2.23	n(t-2)	1.74
AE(t-2)	1.47	AE(t-2)p(t-1)	1.67
p(t-2)	0.97	n(t-10)n(t-10)	0.95
p(t-9)	0.72	Dst(t-1)p(t-9)	0.86
$\sum$ERR	8.15	$\sum$ERR	8.40

Table 25. Table showing the control parameters according to their ERR for Hiss emissions at L-shell 5-7 and MLT 20-00

Hiss wave at L = 5-7 and MLT = 20-00			
Linear		Quadratic Nonlinear	
Control Parameter	ERR(%)	Control Parameter	ERR(%)
Dst(t-1)	5.73	$B_T \sin^6(\theta/2)$(t-3)p(t-1)	8.36
p(t-1)	3.04	n(t-2)	2.43
V(t-10)	2.54	AE(t-9)n(t-4)	1.76
AE(t-9)	1.25	$B_T \sin^6(\theta/2)$(t-2)p(t-1)	1.29
V(t-4)	0.69	$B_T \sin^6(\theta/2)$(t-9)p(t-7)	0.93
$\sum$ERR	13.25	$\sum$ERR	14.77

Table 26. Table showing the control parameters according to their ERR for EMS emissions at L-shell 4-5 and MLT 00-04

EMS wave at L = 4-5 and MLT = 00-04			
Linear		Quadratic Nonlinear	
Control Parameter	ERR(%)	Control Parameter	ERR(%)
Dst(t-9)	3.25	Dst(t-8)V(t-10)	4.40
$B_T \sin^6(\theta/2)$(t-10)	1.26	AE(t-10)	1.91
V(t-8)	0.29	Dst(t-8)	0.91
Dst(t-8)	0.27	Dst(t-6)n(t-3)	0.44
p(t-5)	0.27	AE(t-10)n(t-9)	0.35
$\sum$ERR	5.33	$\sum$ERR	8.01

Table 27. Table showing the control parameters according to their ERR for EMS emissions at L-shell 4-5 and MLT 04-08

EMS wave at L = 4-5 and MLT = 04-08			
Linear		Quadratic Nonlinear	
Control Parameter	ERR(%)	Control Parameter	ERR(%)
$B_T \sin^6(\theta/2)$(t-7)	1.34	$B_T \sin^6(\theta/2)$(t-7)	1.43
Dst(t-10)	0.68	Dst(t-10)V(t-9)	1.04
$B_T \sin^6(\theta/2)$(t-3)	0.46	p(t-3)n(t-10)	0.78
AE(t-7)	0.44	Dst(t-5)V(t-6)	0.56
$B_T \sin^6(\theta/2)$(t-1)	0.37	Dst(t-10)AE(t-7)	0.54
$\sum$ERR	3.29	$\sum$ERR	4.34

Table 28. Table showing the control parameters according to their ERR for EMS emissions at L-shell 4-5 and MLT 08-12

EMS wave at L = 4-5 and MLT = 08-12			
Linear		Quadratic Nonlinear	
Control Parameter	ERR(%)	Control Parameter	ERR(%)
AE(t-6)	2.77	AE(t-6)	2.77
AE(t-1)	1.96	AE(t-1)	1.96
n(t-1)	1.27	n(t-1)V(t-4)	1.29
Dst(t-10)	0.57	$B_T \sin^6(\theta/2)$(t-2)n(t-6)	1.11
$B_T \sin^6(\theta/2)$(t-10)	0.32	Dst(t-9)Dst(t-9)	0.79
$\sum$ERR	6.88	$\sum$ERR	7.92

Table 29. Table showing the control parameters according to their ERR for EMS emissions at L-shell 4-5 and MLT 12-16

EMS wave at L = 4-5 and MLT = 12-16			
Linear		Quadratic Nonlinear	
Control Parameter	ERR(%)	Control Parameter	ERR(%)
AE(t-3)	5.78	AE(t-4)AE(t-4)	6.07
n(t-4)	3.09	AE(t-2)n(t-1)	1.82
$B_T \sin^6(\theta/2)$(t-3)	0.98	n(t-2)	1.35
p(t-4)	0.59	AE(t-1)AE(t-1)	1.19
AE(t-4)	0.59	AE(t-4)	0.92
$\sum$ERR	11.03	$\sum$ERR	11.35

Table 30. Table showing the control parameters according to their ERR for EMS emissions at L-shell 4-5 and MLT 16-20

EMS wave at L = 4-5 and MLT = 16-20			
Linear		Quadratic Nonlinear	
Control Parameter	ERR(%)	Control Parameter	ERR(%)
Dst(t-2)	2.16	Dst(t-2)V(t-1)	2.37
$B_T \sin^6(\theta/2)$(t-1)	1.14	$B_T \sin^6(\theta/2)$(t-1)n(t-8)	1.08
AE(t-2)	0.81	AE(t-2)n(t-8)	0.94
n(t-2)	0.56	p(t-7)p(t-7)	0.75
$B_T \sin^6(\theta/2)$(t-7)	0.46	$B_T \sin^6(\theta/2)$(t-6)n(t-2)	0.65
$\sum$ERR	5.14	$\sum$ERR	5.79

Table 31. Table showing the control parameters according to their ERR for EMS emissions at L-shell 4-5 and MLT 20-00

EMS wave at L = 4-5 and MLT = 20-00			
Linear		Quadratic Nonlinear	
Control Parameter	ERR(%)	Control Parameter	ERR(%)
Dst(t-10)	2.31	Dst(t-10)V(t-10)	2.63
$B_T \sin^6(\theta/2)$(t-1)	0.51	$B_T \sin^6(\theta/2)$(t-2)p(t-1)	0.63
p(t-1)	0.35	$B_T \sin^6(\theta/2)$(t-1)V(t-10)	0.52
Dst(t-5)	0.29	AE(t-1)$B_T \sin^6(\theta/2)$(t-7)	0.36
$B_T \sin^6(\theta/2)$(t-7)	0.16	Dst(t-5)V(t-5)	0.35
$\sum$ERR	3.63	$\sum$ERR	4.49

Table 32. Table showing the control parameters according to their ERR for EMS emissions at L-shell 5-7 and MLT 22-05

EMS wave at L = 5-7 and MLT = 22-05			
Linear		Quadratic Nonlinear	
Control Parameter	ERR(%)	Control Parameter	ERR(%)
Dst(t-1)	2.60	$B_T \sin^6(\theta/2)$(t-1)p(t-1)	3.14
$B_T \sin^6(\theta/2)$(t-1)	1.12	n(t-2)	1.30
n(t-2)	0.93	Dst(t-10)AE(t-8)	1.14
V(t-10)	0.59	Dst(t-9)$B_T \sin^6(\theta/2)$(t-9)	0.51
p(t-1)	0.48	AE(t-9)$B_T \sin^6(\theta/2)$(t-2)	0.37
$\sum$ERR	5.71	$\sum$ERR	6.45

Table 33. Table showing the control parameters according to their ERR for EMS emissions at L-shell 5-7 and MLT 05-11

EMS wave at L = 5-7 and MLT = 05-11			
Linear		Quadratic Nonlinear	
Control Parameter	ERR(%)	Control Parameter	ERR(%)
$B_T \sin^6(\theta/2)$(t-6)	0.88	AE(t-10)n(t-2)	0.93
AE(t-10)	0.68	p(t-10)V(t-4)	0.80
$B_T \sin^6(\theta/2)$(t-2)	0.46	Dst(t-6)AE(t-10)	0.74
p(t-10)	0.43	$B_T \sin^6(\theta/2)$(t-1)n(t-3)	0.58
Dst(t-2)	0.28	AE(t-9)	0.54
$\sum$ERR	2.73	$\sum$ERR	3.60

Table 34. Table showing the control parameters according to their ERR for EMS emissions at L-shell 5-7 and MLT 11-15

EMS wave at L = 5-7 and MLT = 11-15			
Linear		Quadratic Nonlinear	
Control Parameter	ERR(%)	Control Parameter	ERR(%)
AE(t-1)	4.32	AE(t-2)V(t-10)	4.52
n(t-7)	2.39	V(t-5)	2.14
V(t-5)	0.54	$B_T \sin^6(\theta/2)$(t-2)V(t-1)	1.22
AE(t-2)	0.48	AE(t-2)p(t-10)	0.98
AE(t-10)	0.44	Dst(t-10)AE(t-10)	0.78
$\sum$ERR	8.16	$\sum$ERR	9.64

Table 35. Table showing the control parameters according to their ERR for EMS emissions at L-shell 5-7 and MLT 15-19

EMS wave at L = 5-7 and MLT = 15-19			
Linear		Quadratic Nonlinear	
Control Parameter	ERR(%)	Control Parameter	ERR(%)
AE(t-2)	2.30	AE(t-2)V(t-10)	3.07
n(t-2)	2.26	n(t-2)	2.02
p(t-2)	0.65	p(t-1)n(t-2)	0.65
AE(t-9)	0.23	AE(t-2)AE(t-2)	0.60
$B_T \sin^6(\theta/2)$(t-1)	0.23	Dst(t-4)p(t-8)	0.52
$\sum$ERR	5.68	$\sum$ERR	6.86

Table 36. Table showing the control parameters according to their ERR for EMS emissions at L-shell 5-7 and MLT 19-23

EMS wave at L = 5-7 and MLT = 19-23			
Linear		Quadratic Nonlinear	
Control Parameter	ERR(%)	Control Parameter	ERR(%)
Dst(t-3)	1.99	Dst(t-3)V(t-6)	2.66
$B_T \sin^6(\theta/2)$(t-8)	0.75	$B_T \sin^6(\theta/2)$(t-8)	0.87
n(t-10)	0.53	AE(t-8)n(t-4)	0.67
p(t-1)	0.49	n(t-6)	0.64
AE(t-6)	0.39	Dst(t-8)p(t-8)	0.62
$\sum$ERR	4.15	$\sum$ERR	5.45

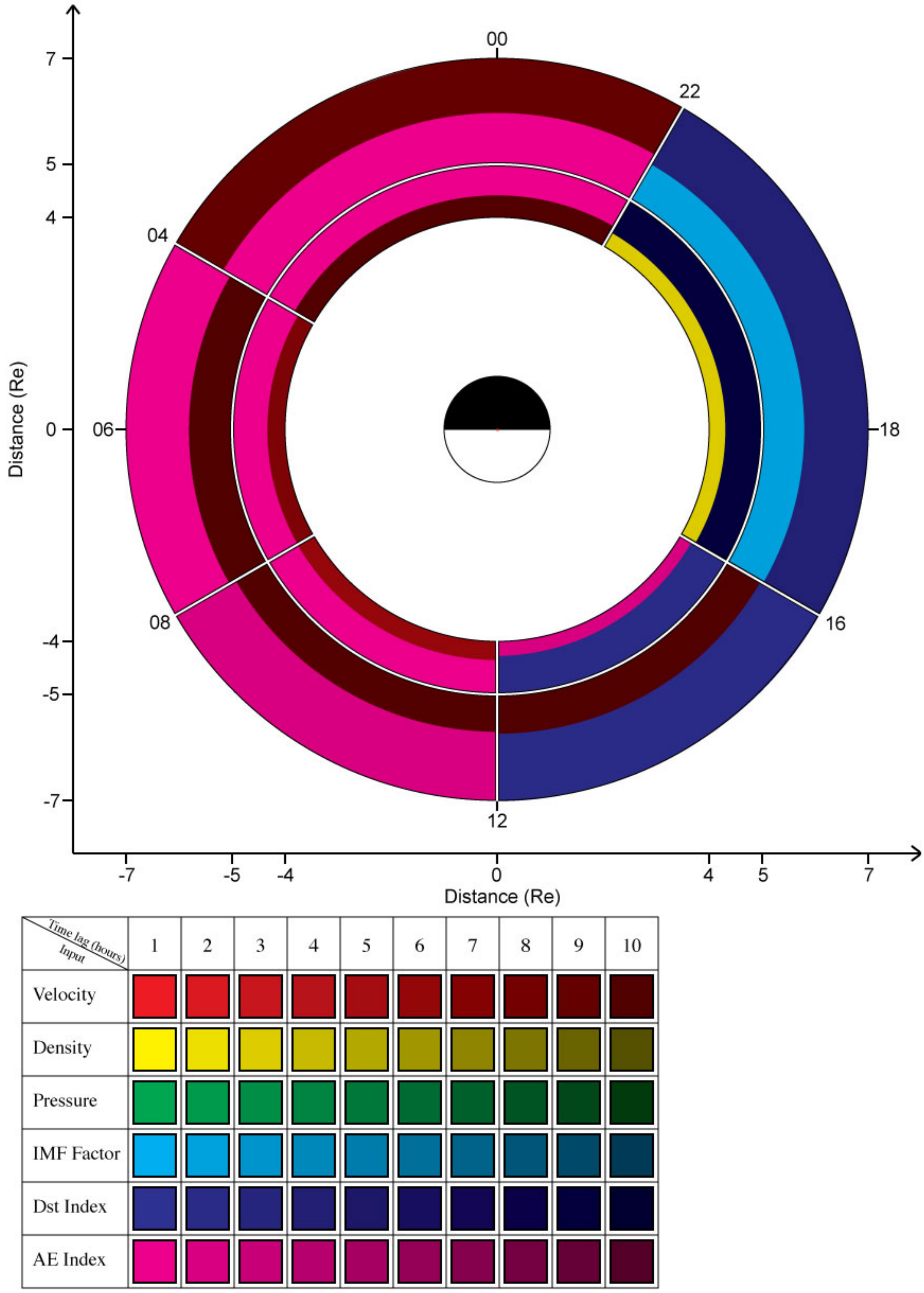

Figure 1. The Figure depicts the ERR results of LBC emissions. It shows the equatorial plane of the inner magnetosphere in distance and MLT, where each sector, or spatial bin, is delineated by the white boundary. For each individual sector, there are two colours that represent the top two control parameters of the emission type according to their ERR. The proportion of radial length that each of the two colours occupy signifies their relative contribution to the LBC emissions.

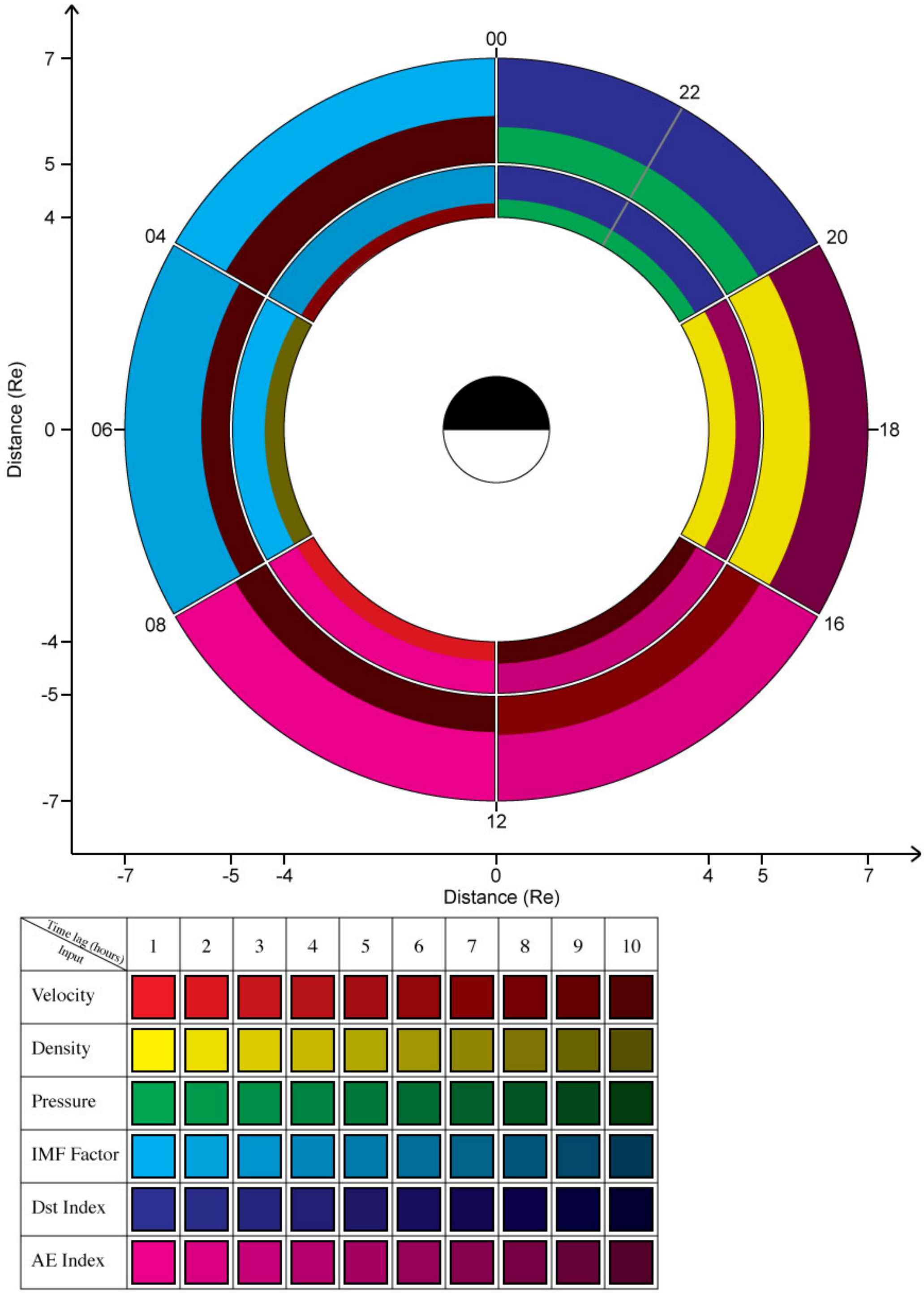

Figure 2. The figure follows the same format as Figure 1 but for hiss emissions.

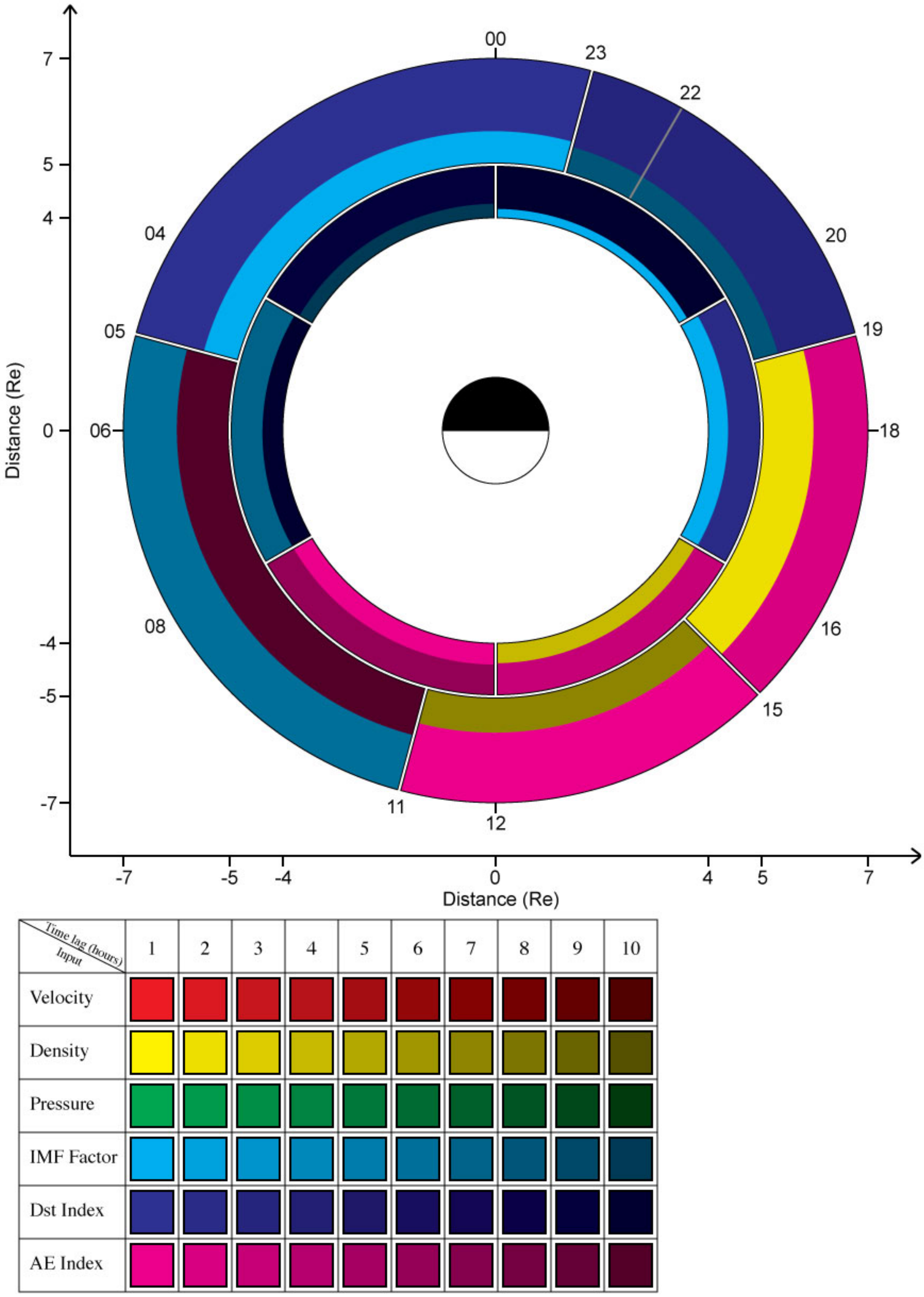

Figure 3. The figure follows the same format as Figure 1 but for EMS emissions.